AGU PUBLICATIONS

JGR

Journal of Geophysical Research: Solid Earth

RESEARCH ARTICLE
10.1002/2015JB012561

Key Points:
- We model injection into reservoir above basement faults including full poroelastic coupling
- Pore pressure diffusion increases seismicity rates on hydraulically connected and conductive faults
- Indirect poroelastic stressing may induce seismicity on hydraulically isolated faults

Correspondence to:
K. W. Chang,
k1chang@stanford.edu

Citation:
Chang, K. W., and P. Segall (2016), Injection-induced seismicity on basement faults including poroelastic stressing, *J. Geophys. Res. Solid Earth*, *121*, doi:10.1002/2015JB012561.

Received 5 OCT 2015
Accepted 22 MAR 2016
Accepted article online 28 MAR 2016

Injection-induced seismicity on basement faults including poroelastic stressing

K. W. Chang[1] and P. Segall[1]

[1]Department of Geophysics, Stanford University, Stanford, California, USA

Abstract Most significant induced earthquakes occur on faults within the basement beneath sedimentary cover. In this two-dimensional plane strain numerical study, we examine the full poroelastic response of basement faults to fluid injection into overlying strata, considering both (1) the permeability of the fault zone and (2) the hydraulic connectivity of the faults to the target horizon. Given hydraulic and mechanical properties, we compute the spatiotemporal change in Coulomb stress, which we separate into (1) the change in poroelastic stresses $\Delta\tau_s + f\Delta\sigma_n$, where $\Delta\tau_s$ and $\Delta\sigma_n$ are changes in shear and normal stress ($\Delta\tau_s > 0$ and $\Delta\sigma_n > 0$ both favor slip), and (2) the change in pore pressure $f\Delta p$. Pore pressure diffusion into hydraulically connected, permeable faults dominates their mechanical stability. For hydraulically isolated or low-permeability faults, however, poroelastic stresses transmitted to deeper basement levels can trigger slip, even without elevated pore pressure. The seismicity rate on basement fault zones is predicted using the model of Dieterich (1994). High seismicity rates can occur on permeable, hydraulically connected faults due to direct pore pressure diffusion. Lower rates are predicted on isolated steeply dipping normal faults, caused solely by poroelastic stressing. In contrast, seismicity on similarly oriented reverse faults is inhibited.

1. Introduction

Subsurface fluid injection has become the standard method for disposal of brine produced along with oil and gas in the energy industry. Over the past few years the central and eastern United States has experienced elevated levels of seismic activity, and most of these recent earthquakes are observed near industrial activities, including deep injection of wastewater [*Horton*, 2012; *Kim*, 2013; *Ellsworth*, 2013; *Kerenan et al.*, 2013; *NRC*, 2013; *Frohlich et al.*, 2014]. The majority of induced earthquakes associated with fluid injection occurred within basement rocks, 1 to 4 km deeper than the target formations [*Nicholson and Wesson*, 1990; *Seeber and Armbruster*, 1993; *Seeber et al.*, 2004; *Horton*, 2012; *Kim*, 2013]. Large earthquakes require large faults, and where sedimentary cover is relatively thin, large faults must involve the basement. In this study, therefore, we focus attention on how fluid injection perturbs pore pressures and stresses in basement rocks beneath the target formation.

In order to achieve safe operation, an important question is how much fluid can be injected without mechanical failure of the securing formations, i.e., what is the storage capacity [*Tsang and Apps*, 2005]. In 1974, the Safe Drinking Water Act required the U.S. Environmental Protection Agency to set minimum requirements for deep injection wells utilized by the oil and gas industry as well as other wells for disposal of hazardous waste, recently including geological carbon dioxide (CO_2) sequestration [*U.S. Environmental Protection Agency*, 2010]. The environmental regulations limit the increase of pore pressure to below 80% of the lithostatic pressure without upward migration of CO_2 saturated brine into potable aquifers. This concern focused attention on overlying aquitards confining the reservoir or upper aquifers for groundwater [*Birkholzer et al.*, 2009; *Chang et al.*, 2013; *Dai et al.*, 2014; *Bacon et al.*, 2016], as well as faults or fractures within them [*Rinaldi et al.*, 2014]. In terms of seismicity, however, the potential for inducing seismicity in the underlying basement rocks is critical [*Zoback and Gorelick*, 2012; *Vilarrasa and Carrera*, 2015]. Therefore, the analysis of the potential earthquakes induced by fluid injection requires us to consider the hydrological and mechanical properties of basement rocks and faults.

Recently, *Ellsworth* [2013] reviewed induced earthquakes driven by either direct increase of pore pressure along faults or indirect change in stresses on faults. Hydrological modeling studies show that the presence of well-oriented and critically stressed faults within either the target formation or the basement increases the probability of earthquakes associated with injection-induced pore pressure changes [*Zhang et al.*, 2013;

Kerenan et al., 2014]. Most models neglect poroelastic stress changes associated with injection, assuming that direct pore pressure changes are the dominant effect in destabilizing faults. However, indirect transfer of stress may perturb faults even without direct diffusion of pore pressure into the faults. Fluid injection or extraction can induce seismicity by changing stress fields in rocks adjacent to the storage formation due to poroelastic coupling [*Segall*, 1989; *Segall et al.*, 1994; *Segall and Lu*, 2015]. Poroelasticity describes the physical process of rock deformation as well as fluid flow through deformable pores and more accurately estimates the changes in stress and pore pressure within the crust. The Coulomb criterion has been widely used to characterize the condition under which failure occurs in rocks [*Jaeger and Cook*, 1979], and the Coulomb stress τ is used as a measure of proximity to failure for given pressure and stress state [*Harris et al.*, 1995]. One goal of this study is to examine the effect of full poroelastic coupling on the Coulomb stress changes for different types of basement faults categorized by their permeability as well as hydraulic connectivity of the basement faults to the target reservoir. Note that we compute changes in Coulomb stress from some initial stress state, as opposed to absolute stress, to determine whether fluid injection promotes or inhibits slip on faults of a given orientation.

Pore pressure diffusion is thought to be the principal mechanism for inducing seismicity [*Healy et al.*, 1968; *Raleigh et al.*, 1976], and thus, the onset of seismicity has been fit by expressions of the form $r_t \sim \sqrt{ct}$ [*Rothert and Shapiro*, 2003; *Shapiro et al.*, 2007; *Shapiro and Dinske*, 2009]. However, laboratory data and models based on rate and state friction show that time-dependent nucleation of slip is controlled by both initial conditions and applied stress history [*Dieterich*, 1979, 1986; *Dieterich and Kilgore*, 1994; *Beeler and Lockner*, 2003, 1994]. *Segall and Lu* [2015] recently studied the effects of rate-dependent earthquake nucleation in a poroelastic medium with uniform hydrologic and mechanical properties. The second goal of this work is to explore how different types of basement faults influence the spatiotemporal evolution of seismicity. Our analysis emphasizes that poroelastic stresses on the basement faults can reduce stability and may induce seismicity, depending on fault properties and geometry.

Here we examine the poroelastic response of basement faults to fluid injection into a geologically layered sequence, including full poroelastic coupling and time-dependent earthquake nucleation. Section 2 describes the model geometry and governing equations. In section 3.1 we explore the deformation-diffusion process for fluid injection into the reservoir with overlying mudrock and underlying basement rock. In section 3.2 we quantify the effect of basement faults on the spatiotemporal evolution of pore pressure as well as normal and shear stresses as a function of fault permeability and geometry. In section 3.3 we compare poroelastic effects to the direct pore pressure effect on Coulomb strength. In section 3.4 we estimate the seismicity rate on basement faults and discuss how fault properties, i.e., permeability and geometry, affect the spatiotemporal evolution of induced seismicity. In section 4.1 we discuss how different faulting states affect the magnitude of the Coulomb stress change as well as the seismicity rate. Finally, in section 4.2 we test how variations in fault friction affect the relative significance of poroelastic stressing. This generic study models a typical layered formation including basement rock and does not focus on a specific injection site.

2. Model Problem

Poroelasticity involves coupling of equations for deformation of the solid matrix with those governing pore fluid flow. *Biot* [1941] first introduced the governing equations for the deformation of a homogeneous, isotropic, and linearly elastic fluid-saturated medium. Flow of pore-filled fluids is described by diffusion of pore pressure p and the mass of diffusing fluids m per unit volume of the porous medium [*Rice and Cleary*, 1976]. The governing equations of poroelasticity can be derived on the basis of the following assumptions: (1) the medium is porous, linear elastic; (2) saturated fluid flow follows Darcy's law; (3) fluid mass is conserved; and (4) isothermal conditions exist. In this study, we consider basin-scale heterogeneity by modeling a three-layer system in two-dimensional coordinates, $\mathbf{x} = (x_1, x_3)$ with spatial variations in both mechanical and hydrological properties.

2.1. Governing Equations

The linear theory of poroelasticity for an isotropic, fluid-saturated porous medium relates the strains ϵ_{ij} and the increment in fluid mass per unit volume of solid Δm as a linear combination of stresses σ_{ij} and pore pressure p [*Biot*, 1941; *Rice and Cleary*, 1976; *Wang*, 2000]

$$2G\epsilon_{ij} = \sigma_{ij} - \frac{\nu}{1+\nu}\sigma_{kk}\delta_{ij} + \frac{(1-2\nu)\alpha}{1+\nu}p\delta_{ij}, \tag{1}$$

$$\Delta m = \frac{9\rho_f \left(\nu_u - \nu\right)}{2GB^2 \left(1+\nu\right)\left(1+\nu_u\right)} \left(\frac{B\sigma_{kk}}{3} + p\right), \tag{2}$$

where G (Pa) is the shear modulus, ν (–, dimensionless) is the drained Poisson's ratio, ν_u is under undrained conditions, ρ_f (kg/m^3) is the fluid density in the undeformed, reference state, B (–) is the Skempton's coefficient giving the ratio of the change in pore pressure to the change in mean normal stress for undrained conditions ($p = -B\sigma_{kk}/3$), and α (–) is Biot-Willis coefficient relating change in pore pressure to volumetric strain. The constitutive equations (1) and (2) are combined with field equations for conservation of momentum and fluid mass

$$\sigma_{ij,j} + \mathbf{f}_i = 0, \tag{3}$$

$$\frac{\partial m}{\partial t} + \nabla \cdot \mathbf{q} = 0, \tag{4}$$

where $\mathbf{f}_i$ is the component of the body force per unit volume of the bulk material and $\mathbf{q}$ is the mass flux of pore fluid.

The force equilibrium equation (3) can be expressed in terms of displacement u_i and pore pressure p [e.g., *Segall*, 2010]

$$\nabla \cdot \left[G\left(\mathbf{x}\right)\nabla \mathbf{u}\right] + \nabla\left[\frac{G\left(\mathbf{x}\right)}{1-2\nu\left(\mathbf{x}\right)}\right]\nabla \cdot \mathbf{u} - \alpha(\mathbf{x})\nabla p + \mathbf{f} = 0. \tag{5}$$

In equation (5), the pore pressure gradients act as body forces and induce deformations of the solid.

To derive the governing equation for single-phase transient flow in a heterogeneous and isotropic compressible porous medium, we need to employ conservation of fluid mass given by (4) and Darcy's law $\mathbf{q} = -(\rho_f \kappa/\eta)\nabla p$, where κ (m^2) is permeability and η (Pa s) is the fluid viscosity, and the constitutive equation (2). The flow equation can be written in the form of an inhomogeneous diffusion equation for pore pressure in which the divergence of the displacements acts as a source term [*Wang*, 2000; *Segall*, 2010]

$$S_\epsilon\left(\mathbf{x}\right)\frac{\partial p}{\partial t} - \frac{1}{\eta}\nabla \cdot \left[\kappa\left(\mathbf{x}\right)\nabla p\right] = -\alpha(\mathbf{x})\frac{\partial}{\partial t}\left(\nabla \cdot \mathbf{u}\right), \tag{6}$$

and S_ϵ (Pa^{-1}) is the constrained specific storage [*Wang*, 2000] given by

$$S_\epsilon = \frac{\alpha^2\left(1-2\nu\right)\left(1-2\nu_u\right)}{2G\left(\nu_u - \nu\right)}. \tag{7}$$

S_ϵ represents the fluid volume change per unit control volume per pressure change while holding the control volume constant. The storage capacity can be quantified by the specific storage S, representing the change of fluid mass due to increase in pore pressure within a unit volume, expressed mathematically $S \sim \Delta m/\Delta p$ [*Narasimhan and Kanehiro*, 1980]. Smaller S implies a less compressible fluid-saturated solid and limits the increment of pore volume due to pore pressure increase. A general form of the specific storage under arbitrary stress-strain conditions needs to consider the change in the total stresses as well as the change in fluid pressure [*Green and Wang*, 1990].

Note that equations (5) and (6) are fully coupled—that is, a change in volumetric strain produces a change in pore pressure (solid-to-fluid coupling) and conversely gradients in pore pressure induce deformation of the porous matrix (fluid-to-solid coupling). Mathematically, this coupling is manifest by the presence of ∇p in the equilibrium equations (5) and $\nabla \cdot \mathbf{u}$ in the flow equation (6).

The diffusion equation can also be expressed as follows [*Wang*, 2000]

$$S_\sigma\left(\mathbf{x}\right)\frac{\partial}{\partial t}\left(\frac{B}{3}\sigma_{kk} + p\right) - \frac{1}{\eta}\nabla \cdot \left[\kappa\left(\mathbf{x}\right)\nabla p\right] = 0, \tag{8}$$

where the mean normal stress acts as a source term and S_σ (Pa^{-1}) is the specific storage at constant applied stress, or the unconstrained specific storage [*Wang*, 2000], defined as

$$S_\sigma = \frac{\alpha^2(1-2\nu)^2(1+\nu_u)}{2G(1+\nu)(\nu_u - \nu)}. \tag{9}$$

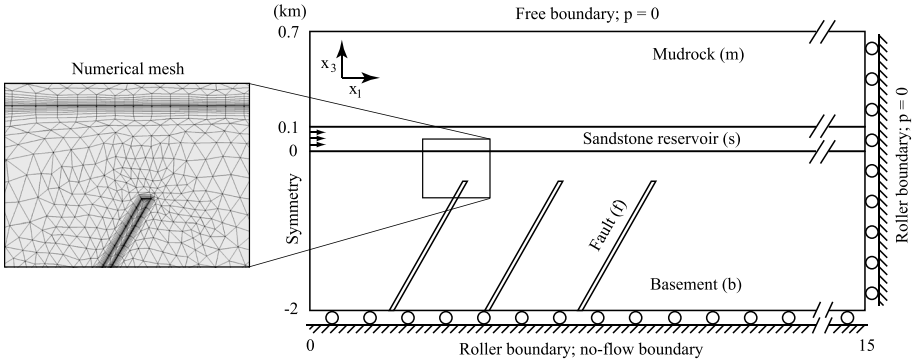

Figure 1. Schematic description of the model. The formation properties are given in Table 1. Laterally and vertically extensive geometry ($L \sim 5\sqrt{4c_s \Delta t}$; $H_b \sim 12\sqrt{4c_b \Delta t}$) minimizes boundary effects on pore pressure. Isolated faults are shown; the upper limits of the faults are extended to $x_3 = 0$ m for faults connected to the sandstone reservoir. A refined mesh is used to resolve strong gradients in pore pressure and stresses at faults and lithologic boundaries.

Under the assumption of uniaxial strain and constant vertical stress ($\epsilon_{11} = \epsilon_{22} = 0, \sigma_{33} = 0$), equations (6) and (8) reduce to an uncoupled transient flow equation

$$S_u(\mathbf{x}) \frac{\partial p}{\partial t} - \frac{1}{\eta} \nabla \cdot [\kappa(\mathbf{x}) \nabla p] = 0, \tag{10}$$

where S_u (Pa^{-1}) is the uniaxial specific storage [*Wang*, 2000] defined as

$$S_u = \frac{\alpha^2 (1-2\nu)^2 (1-\nu_u)}{2G(1-\nu)(\nu_u - \nu)}. \tag{11}$$

In this limit there is only one-way, fluid-to-solid coupling.

In a homogeneous domain, we define hydraulic diffusivity as

$$c = \frac{\kappa}{\eta S}. \tag{12}$$

The constrained specific storage S_ϵ is smallest because the volume is held constant, which means that the volume of fluid released is due primarily to fluid compressibility. The unconstrained specific storage S_σ is greatest because the least restraint is placed on the framework as pore pressure is decreased. The uniaxial specific storage S_u lies in between two because only lateral strain is held constant. Given mechanical properties, we can calculate the value of the specific storage defined by (7) and (9) in fully coupled equations or (11) in an one-way coupled (uncoupled) equation and predict the pore pressure field $p(\mathbf{x}, t)$ for each model. Note further that the pore pressure distribution will be different in the uncoupled formulation (11) compared to the fully coupled case even though mechanical and hydrological properties are identical (refer to section 3.1).

2.2. Layered Geometry With Basement Faults

We consider a three-layer geometry comprising a laterally extensive sandstone reservoir overlain by a thick mudrock (shale, siltstone, or other fine-grained clastic rock) sequence and underlain by basement rocks including faults as shown in Figure 1. The two-dimensional, plane strain ($\partial(\cdot)/\partial x_2 = 0$) domain has origin at the bottom of the injector (depth of 3 km). The initial conditions for pore pressure and stresses are given by

$$\sigma_{ij}(\mathbf{x}, t = 0) = 0, \tag{13}$$

$$p(\mathbf{x}, t = 0) = 0. \tag{14}$$

Note that since this study considers perturbations from an initial self-equilibrated stress state, the affect of gravity on deformation can be neglected [*Segall*, 2010, chap. 9]. In addition, the change in stress due to the

weight of the injected/extracted fluid is small compared to poroelastic stress changes [*Segall*, 1985]. Assuming fluid injection at $x_1 = 0$ with constant mass rate Q per unit length of the reservoir thickness (kg/m s), the hydraulic boundary conditions are given by

$$\frac{\kappa_s}{\mu}\left(\frac{\partial p}{\partial x}\right)_{x_1=0} = \begin{cases} -Q \;;\; 0 < x_3 \le H_s, & 0 \le t \le \Delta t \\ 0 \;\;\;;\; x_3 < 0,\; x_3 > H_s \end{cases}, \tag{15}$$

$$\lim_{x_1\to\infty}\lim_{x_3\to\infty} p = 0, \tag{16}$$

where H_s (m) is the thickness of the sandstone reservoir and Δt (days) is the injection period. We adopt a laterally extensive geometry in which the reservoir length is 5 times the characteristic diffusive length in the sandstone reservoir ($L = 15$ km $\sim 5\sqrt{4c_s\Delta t}$) for $\Delta t = 30$ days, and the basement thickness is 12 times the length scale in the basement ($H_b = 2$ km $\sim 12\sqrt{4c_b\Delta t}$). Longer injection periods, e.g., years or decades as common for wastewater disposal [*Rubinstein and Mahani*, 2015], require larger model domains in order to neglect boundary effects.

Mechanically, the bottom and side boundaries are fixed in the normal direction to boundaries but free to move in the parallel direction

$$\lim_{x_j\to\infty} \hat{n}\cdot\mathbf{u} = 0, \tag{17}$$

where $\hat{n}$ is the normal vector and $\mathbf{u}$ is displacement. The top of the domain is traction free (Figure 1). The spatial variation of the physical properties in this layered geometry is given by

$$\kappa(\mathbf{x}) = \begin{cases} \kappa_m \;;\; x_3 > H_s \\ \kappa_s \;;\; 0 \le x_3 \le H_s \\ \kappa_b \;;\; x_3 < 0 \end{cases}, \tag{18}$$

$$S(\mathbf{x}) = \begin{cases} S_m \;;\; x_3 > H_s \\ S_s \;;\; 0 \le x_3 \le H_s \\ S_b \;;\; x_3 < 0 \end{cases}, \tag{19}$$

where the subscripts m, s, and b represent mudrock, sandstone, and basement and S is either S_σ for coupled models using (8) or S_u for uncoupled models using (10). Petrophysical and mechanical properties of the overlying mudrock and the sandstone reservoir are from the Cranfield site in southwestern Mississippi near the border of Louisiana in which CO_2 had been injected as a pilot project for CO_2 storage [*Kim and Hosseini*, 2013]. The entire sequence overlying the sandstone reservoir is represented as a single homogeneous mudrock sequence with a thickness of 600 m. This mudrock acts as a confining unit for fluid injection with a relatively low permeability but considerable compressibility. This setting minimizes the effect of permeable mudrock on lateral pressure propagation; however, the nonzero permeability and high compressibility cause dissipation of injection-induced overpressure into the mudrock [*Chang et al.*, 2013].

To investigate the poroelastic response of basement faults to fluid injection, we include a set of faults within the basement as shown in Figure 1. In this study, we consider extensional (normal) faults with dip angle θ=60°, which are assumed to be well oriented for slip in the ambient stress field, and compute normal and shear stresses on the faults. Note that unfavorably oriented faults are unlikely to slip with modest perturbations in pore pressure and stress. We consider rather end-member cases in which faults are assumed to be either high-permeability conduits ($\kappa_f/\kappa_b = 5\times10^3$) or low-permeability seals ($\kappa_f/\kappa_b = 5\times10^{-5}$). Hydrological properties of the basement rock and faults are based on *Zhang et al.* [2013], and mechanical properties are from *Stanislavsky and Garven* [2002] and *Willson et al.* [2007] (refer to Table 1).

2.3. Seismicity Rate Model

Seismicity is modeled as a sequence of earthquake nucleation events in which the distribution of initial conditions over the population of nucleation sources and stressing history controls the timing of earthquakes. *Dieterich* [1994] derived equations for the seismicity rate R in terms of a seismicity state variable that depends on the change in Coulomb stress. We define the Coulomb stress $\tau = \tau_s + f(\sigma_n + p)$, where τ_s and σ_n are the shear and normal stresses (positive in tension) acting on a fault plane and f is the coefficient of friction.

Table 1. Summary of Model Properties

Model Properties	Mudrock[a]	Sandstone[a]	Basement[b]	Fault[b]	Fluid
κ[c] (m^2)	1×10^{-19}	6.4×10^{-14}	2×10^{-17}	1×10^{-13}, 1×10^{-21}	-
ϕ (–)	0.1	0.25	0.05	0.02	-
G (GPa)	11.5	7.6	25	6	-
ν (–)	0.3	0.15	0.2	0.2	-
ν_u (–)	0.35	0.25	0.25	0.33	-
B (–)	0.8	0.62	0.85	0.62	-
f[d] (–)	0.5	0.6	0.6	0.1, 0.75	-
C (MPa)	75	80	130	0	-
ρ (kg/m^3)	2600	2500	2740	2500	1000
η (Pa s)	-	-	-	-	1×10^{-3}

[a]Mudrock and sandstone properties are based on *Kim and Hosseini* [2013].
[b]Hydrological properties of basement and faults are based on tabulation in *Zhang et al.* [2013], and mechanical properties are based on *Stanislavsky and Garven* [2002] and *Willson et al.* [2007].
[c]The values of fault permeability are given for conductive or sealing faults.
[d]Variable fault frictional coefficients are employed to test the effect of f on poroelastic stressing ($f = 0.75$ for reference case).

For moderate change in $\tau_s/\bar{\sigma}$, where $\bar{\sigma} = \sigma_n + p$ is the effective stress, we assume that $\tau_s/\bar{\sigma}$ is constant. Eliminating the state variable from the *Dieterich* [1994] formulation, *Segall and Lu* [2015] obtain

$$\frac{dR}{dt} = \frac{R}{t_a}\left(\frac{\dot{\tau}}{\dot{\tau}_0} - R\right), \tag{20}$$

where R is the seismicity rate relative to the steady state seismicity rate at reference stressing rate $\dot{\tau}_0$. The characteristic decay time is $t_a \equiv A\bar{\sigma}/\dot{\tau}_0$ where A is a constitutive parameter quantifying the direct effect on slip rate in the rate-state friction law and $\dot{\tau}$ is the Coulomb stressing rate. We take $A = 0.005$, as measured in friction experiments [*Dieterich*, 1994], and $\bar{\sigma} = 10$ MPa at a depth of about 1 km. The background stressing rate $\dot{\tau}_0$ is assumed as 10^{-3} MPa/yr, such that a typical 1 MPa stress drop accumulates in 10^3 years. This leads to a characteristic decay time $t_a = 50$ years. Prediction of R requires the temporal variation of $\dot{\tau}$ at each point on the faults. The ordinary differential equation (20) is solved using the MATLAB solver `ode45` with relative tolerance of 1e−6 and very small absolute tolerance. The poroelastic solution is found at discrete time steps ($t_{\text{step}} = 0.1$ years) using the finite element method (FEM), as described in section 3. To compute the stressing rate, we fit a spline curve to the Coulomb stress from the FEM calculations. The (analytical) time derivative of the spline fit is used to approximate $\dot{\tau}$ (refer to Appendix A). Note that equation (20) assumes that favorably oriented faults are already close to failure and that we only compute the Coulomb stressing rate, which is independent of the background, preinjection stress state.

3. Numerical Results

We performed numerical simulations of the model defined by the governing equations (5) and (6) [or (8)], with initial and boundary conditions ((13)–(17)) and the parameter fields ((18)–(19)). The finite element analysis is conducted with *COMSOL* [2014] using bilinear quadrilateral elements for spatial discretization [*Hughes*, 2000] and a variable step method [*Dreij et al.*, 2011]. The numerical mesh is highly refined near the boundaries of the sandstone reservoir as well as the basement faults to resolve the strong pore pressure gradients typical for this problem as shown in Figure 1.

3.1. Poroelastic Response to Fluid Injection

Before considering the full problem including basement faults, we illustrate the poroelastic effect on pore pressure distribution by comparing the fully coupled model (two-way poroelastic coupling, equation (8)) to the uncoupled one (one-way fluid-to-solid coupling, equation (10)).

The hydrological and mechanical properties of each layer are identical in both models, and we inject the same amount of fluid at a constant rate of 30 kg/s into the sandstone reservoir for 30 days (Δt). The models are run for 300 days so that the postinjection response can be analyzed. We use the same color scheme for contour plots of all parameter fields (red for positive value and blue for negative).

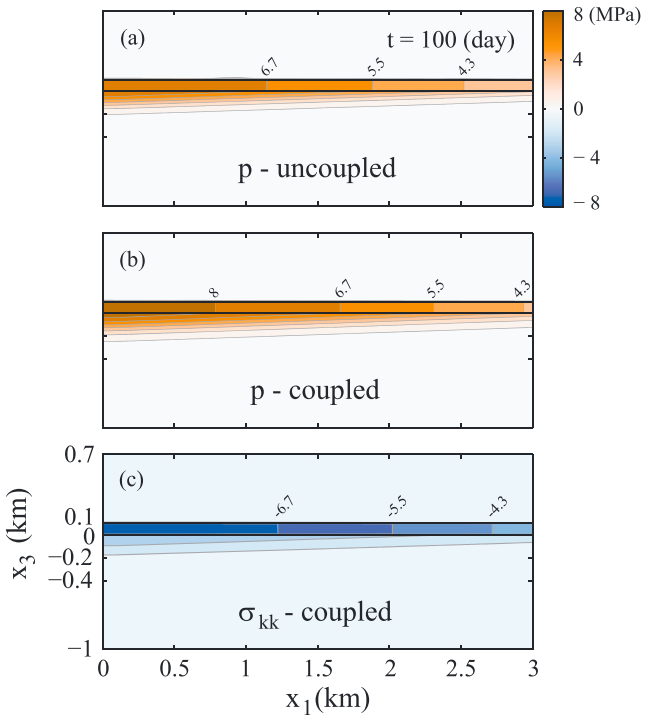

Figure 2. Pore pressure $p(\mathbf{x})$ at $t = 100$ days for (a) uncoupled and (b) fully coupled models. (c) Larger p buildup in the fully coupled, poroelasticity model is due to compressive stress change.

Figures 2a and 2b show the pore pressure in the uncoupled and coupled models at $t = 100$ days when injection has stopped, but pore pressure continues to diffuse into the formations. Given that the injection scenarios are identical and a constant fluid density ρ_f is assumed, both models have the same injected fluid mass. The local change in fluid mass Δm depends on changes in mean stress and pore pressure (refer to Appendix B), and based on the relations (B2) and (B6), the pore pressure change $p(\mathbf{x}, t)$ is given by

$$p(\mathbf{x},t) = \begin{cases} \frac{\Delta m(\mathbf{x},t)}{\rho_f S_\sigma(\mathbf{x})} - \frac{B(\mathbf{x})}{3}\sigma_{kk}(\mathbf{x},t) & ; \text{ coupled} \\ \frac{\Delta m(\mathbf{x},t)}{\rho_f S_u(\mathbf{x})} & ; \text{ uncoupled} \end{cases} . \tag{21}$$

In the coupled, poroelastic model, the pore pressure is determined by two terms: (1) specific storage S_σ associated with the increment in fluid mass Δm and (2) Skempton's coefficient B associated with the perturbation in mean stress. For the uncoupled model, the pore pressure field is determined solely by the change in fluid mass and S_u. Because S_σ is larger than S_u (refer to section 2.1), poroelastic coupling reduces the magnitude of the first term associated with the change in fluid mass. Including poroelastic effects, increase in p causes expansion of the sandstone layer which is resisted by the elastic surroundings. This causes the formation to be driven into compression ($\sigma_{kk}<0$) as shown in Figure 2c. This injection-induced compression causes the second term in (21) to be positive; thus, the poroelastic response to fluid injection results in larger pore pressures in the sandstone reservoir. The uncoupled model cannot capture injection-induced deformation and thus underestimates the magnitude of increase in pore pressure.

3.2. Poroelastic Response of Basement Faults

Before presenting numerical results, we illustrate how the poroelastic response to fluid injection perturbs stress fields in both the formation and basement. Figure 3 describes schematically three physical mechanisms of poroelastic deformation associated with fluid injection. Strong compression develops within the pressurized region (gray) due to poroelastic response to pore pressure buildup, as discussed in section 3.1. Increased pore pressures within the reservoir formation cause the reservoir to expand. This expansion induces horizontal extension of basement rocks below the region with significant pore pressure increase. At the same time lateral expansion of the reservoir induces a smaller horizontal compression in the basement more distant from the injection zone. Without direct diffusion of pore pressure, poroelastic extension/compression of the basement rocks thus perturbs the stress state on basement faults at depth. The boundary between extensional

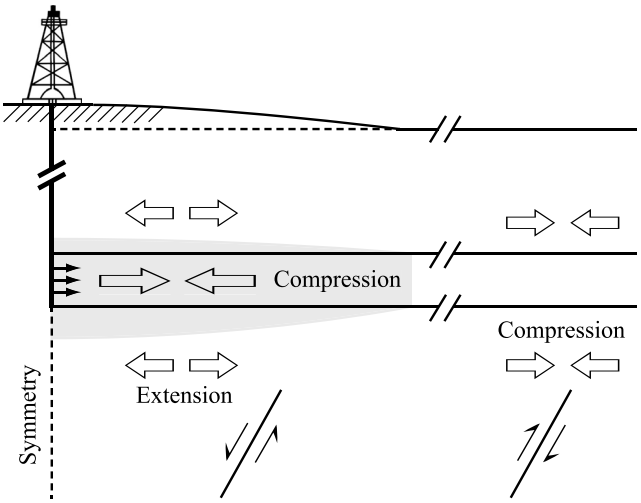

Figure 3. Schematic description summarizing formation deformation and faulting associated with fluid injection. Open arrows indicate horizontal strains in the formation. The gray region indicates pressurized zones due to direct pore pressure diffusion. Poroelastic extension of basement rocks below the pressurized zone near injector enhances normal faulting, while far-field compression favors reverse faulting.

and compressional environments will be determined by the diffusion of pore pressure and thus the hydraulic properties of the formations. In the background extensional environment normal faults near the injector are favored to slip due to increased extension of the basement rocks. In the far field from the injector increased compression inhibits normal faulting. Thus, the full poroelastic response to injection depends on the fault location and orientation, as well as the permeability and hydraulic connectivity to the reservoir.

If the target formation (reservoir) is intersected by faults, they will have a considerable impact on the pore pressure [*Bense and Person*, 2006; *Chang and Bryant*, 2009; *Tueckmantel et al.*, 2012] and stress [*Cocco and Rice*, 2002; *Jha and Juanes*, 2014] distributions in the reservoir. In this study, we focus on faults within the basement hydraulically either connected or isolated from the reservoir. A key goal is to understand the pore pressure and poroelastic stress acting on the faults for different end-member scenarios. The sign and magnitude of poroelastic effects depend on fault geometry (location, dip, or width), injection operations (duration or rate), and poroelastic parameters. However, our goal is not to catalog all possible scenarios. Rather, it is to explore general processes and to emphasize that indirect transfer of poroelastic stresses may destabilize basement faults ("poroelastic stressing"), even without direct pore pressure diffusion into high-permeability faults hydraulically connected to the target reservoir. General insight into effects of expansion of the reservoir can be gained by consideration of Figure 3.

We consider two factors associated with fluid flow in fault zones: (1) the permeability of the fault zones and (2) the hydraulic connectivity of basement faults to the target reservoir. By combining these factors, we introduce four end-member types of faults categorized by permeability (sealing or conductive) and their hydraulic connectivity to the target reservoir (isolated or connected). The petrophysical and mechanical properties of the fault zones are given in Table 1; only permeability κ_f varies. The injection scenario is the same as in section 3.1. For each case, we generate two-dimensional fields of pore pressure $p(\mathbf{x})$, normal $\sigma_n(\mathbf{x})$, and shear stresses $\tau_s(\mathbf{x})$, acting on (or on planes parallel to) the faults, at three different times $\Delta t = 30$ days (end of injection), $t = 100$, and 200 days (postinjection) as shown in Figures 4 to 6. In each figure, the left two columns show the results for conductive faults, while the right two columns show those for sealing faults. The color scale remains the same for the four different cases but varies at different times.

Figure 4 shows the spatial distribution of the pore pressure change multiplied by the friction coefficient, $f\Delta p(\mathbf{x}, t)$, for three time steps. During injection, the pore pressure increases up to 30 MPa, with the largest changes confined within the storage formation except for connected/conductive basement faults. After the end of injection the pore pressure continues to diffuse through the formation and basement.

For isolated/conductive faults shown in Figures 4a to 4c, the vertical enlargement of the pressurized zone is determined by the basement diffusivity. Once the pressure plume approaches the conductive faults, flow into

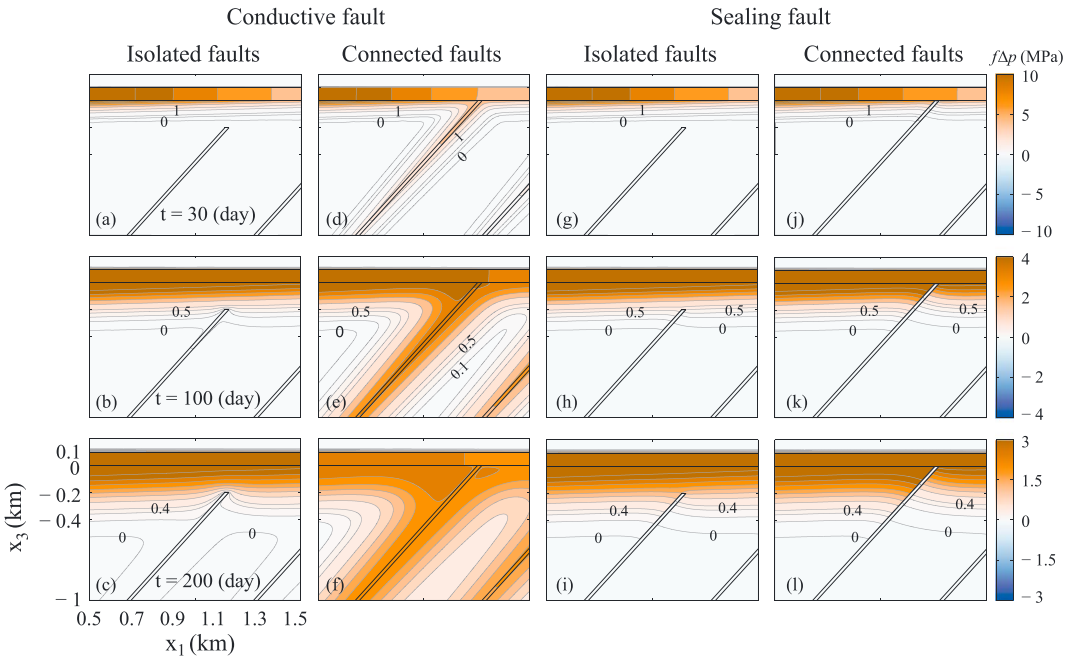

Figure 4. Pore pressure changes $f\Delta p(\mathbf{x})$ from coupled poroelasticity model at t = 30, 100, and 200 days: (a–f) conductive and (g–l) sealing faults.

the faults causes the local pressure gradient to be directed into the faults, distorting the pore pressure contours. On the other hand, if conductive faults are hydraulically connected to the sandstone formation, changes in pore pressure are dominated by flow into the faults as shown in Figures 4d–4f. The faults themselves act as virtual sources for lateral diffusion into the surrounding basement. Flow into the basement also attenuates pore pressure in the target reservoir. Sealing faults act as flow barriers, leading to sharp (but continuous) changes in pore pressure across the faults as shown in Figures 4i–4l. In this case pore pressure gradients in the basement rocks are directed parallel to the faults.

Figures 5 and 6 illustrate close-ups of the normal and shear stresses, $\sigma_n(\mathbf{x}, t)$ and $\tau_s(\mathbf{x}, t)$. The displacement field $\mathbf{u}(\mathbf{x}, t)$ is shown with the shear stress field in Figure 6. For isolated or sealing faults extensional stress ($\sigma_n > 0$, weakening the fault) is observed in the basement far from the reservoir due to injection-induced lateral expansion of the reservoir formation (as predicted from Figure 3). For connected/conductive faults, compressive stress (σ_n<0, strengthening the fault) occurs in and around the fault zone due to pore pressure buildup and hence expansion of the faults (Figures 5d–5f). In the other cases, the normal stress becomes compressive once the pressure plume encounters the faults (e.g., Figures 5a–5c), leading to a time-dependent change from positive to negative normal stress.

Horizontal extension, due to poroelastic dilation of the target formation, induces positive τ_s (normal sense of shear) on the dipping faults (displacements in the positive x_1 direction increasing with increasing distance from the injector). Note that positive shear stresses would act to inhibit faulting in a compressional (reverse) fault system; see section 4.1. For conductive faults that are hydraulically connected to the reservoir (Figures 6d–6f), pore pressure buildup within the faults causes pore pressure gradients outward from the fault zone which must be compensated by stress gradients (refer to equation (5)). The combination of the volumetric expansion within and near the fault zone and the boundary conditions acts to increase shear stress acting on the faults. Because of the symmetry condition at $x_1 = 0$, the displacements near the injector are primarily vertical on the hanging wall side. On the footwall side the expansion of the fault zone can be accommodated more by lateral displacement. These effects cause the shear strains, and hence stresses, to be positive in this normal faulting environment, for the highly conductive and well-connected fault geometry.

Sealing faults divide the pore pressure field, leading to apparent discontinuities in pore pressure across the faults (refer to Figures 4i–4l); pore pressure is, in fact, continuous within the fault zone. The apparent discontinuity leads to pore pressure gradients, and thus equivalent body forces (see equation (5)), that parallel the

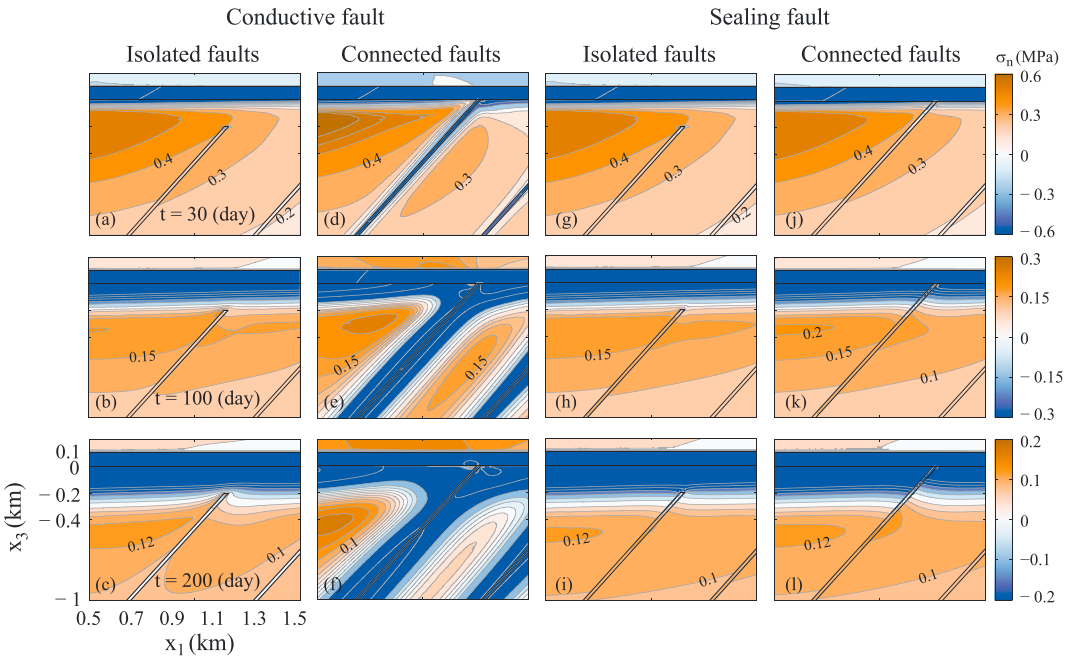

Figure 5. Normal stress, $\sigma_n(\mathbf{x})$, from coupled poroelasticity model at t = 30, 100, and 200 days: (a–f) conductive and (g–l) sealing faults.

fault. This causes stress gradients and apparent discontinuities in shear stress across the faults (τ_s>0 above the fault versus τ_s<0 below the fault zone, Figures 6k and 6l). In detail, the shear stresses are, of course, continuous within the fault zone.

3.3. Coulomb Stress Change

Assuming a constant friction coefficient f, the change in Coulomb stress produced on a failure plane can be defined as

$$\Delta\tau = \Delta\tau_s + f\left(\Delta\sigma_n + \Delta p\right) = \Delta\tau_s + f\Delta\bar{\sigma}, \tag{22}$$

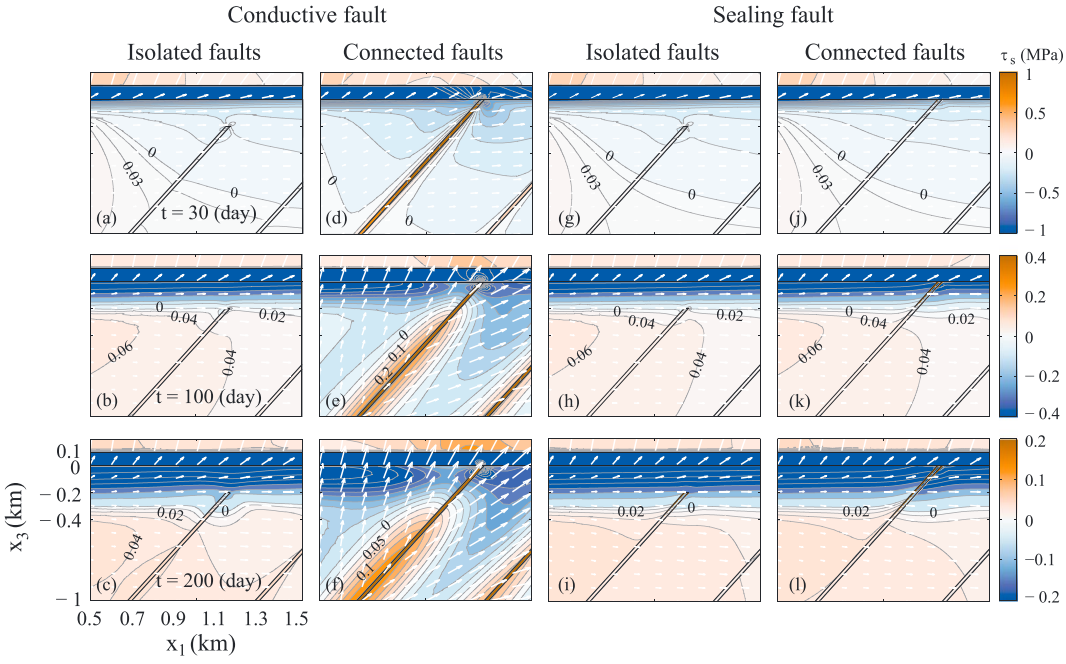

Figure 6. Shear stress $\tau_s(\mathbf{x})$ and displacement vector $\mathbf{u}(\mathbf{x})$ from coupled poroelasticity model at t = 30, 100, and 200 days: (a–f) conductive and (g–l) sealing faults. White vectors show displacements.

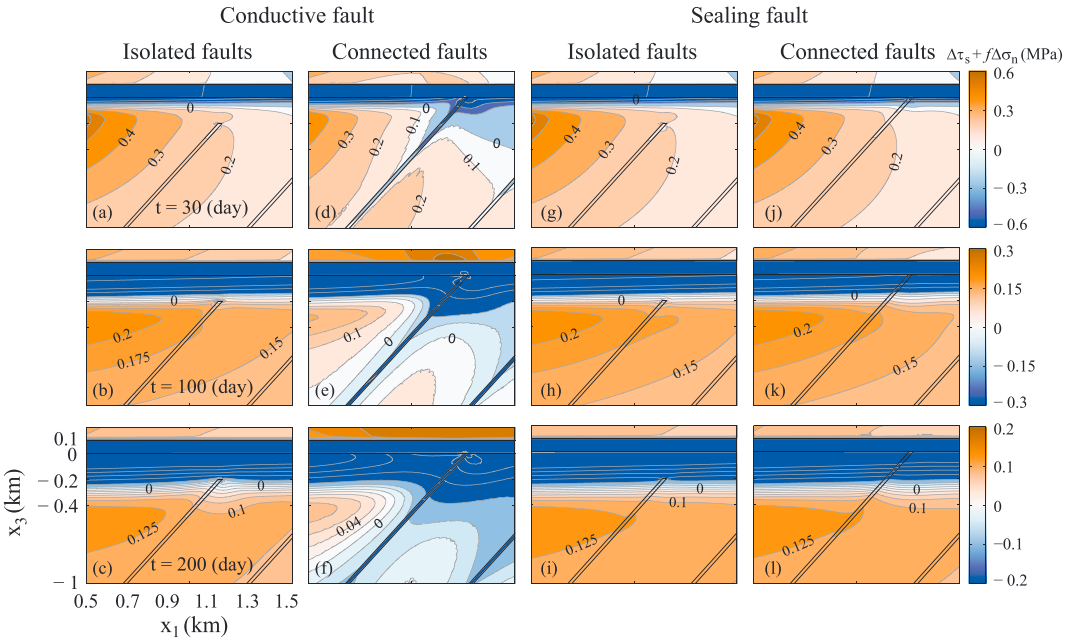

Figure 7. Change in Coulomb stress due to poroelastic stressing $\Delta\tau_s(\mathbf{x}) + f\Delta\sigma_n(\mathbf{x})$ at t = 30, 100, and 200 days: (a–f) conductive and (g–l) sealing faults.

where $\Delta\tau$ is the static change of Coulomb failure stress, $\Delta\tau_s$ is the change in shear stress, $\Delta\sigma_n$ is the change in normal stress, Δp is the change in pore pressure, and $\Delta\bar{\sigma}$ is the change in effective normal stress. Positive values of $\Delta\tau$ imply that the fault plane is closer to failure; positive $\Delta\tau_s$ indicates that the change in shear stress favors slip; positive $\Delta\sigma_n$ means that extension unclamps the fault. To examine the poroelastic response relative to the direct pore pressure effect, we rearrange (22) in terms of the changes in poroelastic stresses and pore pressure as follows:

$$\Delta\tau = \left(\Delta\tau_s + f\Delta\sigma_n\right) + f\Delta p. \tag{23}$$

Figure 7 shows the change in poroelastic stresses, $\Delta\tau_s(\mathbf{x}, t) + f\Delta\sigma_n(\mathbf{x}, t)$. Except for the connected/conductive fault case, there is a positive Coulomb stress change in the basement below the zone of elevated pore pressure. This results from dilation of the reservoir formation which leads to both increases in $\Delta\sigma_n$ and $\Delta\tau_s$ as shown in the previous section. Closer to the reservoir where pore pressures increase, the poroelastic stress change is negative (e.g., Figures 7a–7c) due to negative $\Delta\sigma_n$. If the conductive faults are hydraulically connected to the formation, increased pore pressure leads to expansion of the fault zones and compressive normal stress (Figure 5), decreasing the poroelastic stress (Figures 7d–7f).

Within the pressurized zone, $f\Delta p$ is 1 order of magnitude larger than that of $|(\Delta\tau_s + f\Delta\sigma_n)|$ (refer to Figure 4), which implies that pore pressure changes dominate fault stability in these areas. Outside zones without significant pore pressure changes, poroelastic stresses dominate.

We obtain the total change in Coulomb stress $\Delta\tau(\mathbf{x}, t)$ by summing the direct and poroelastic terms in (23). Figure 8 shows that for the most part the spatial distribution of the Coulomb stress change $\Delta\tau(\mathbf{x})$ is similar to that of the pore pressure change $f\Delta p(\mathbf{x})$ (refer to Figure 4). This implies that stability of basement faults will be dominated by changes in pore pressure, where those changes are nonnegligible. Smaller changes in Coulomb stress beyond the direct impact of elevated pore pressure show that poroelastic stressing can increase failure probability on basement faults at greater depths (Figure 7).

We plot the net Coulomb stress change $\Delta\tau$ along the middle of the fault zone indicated as orange lines in Figures 9a and 9d. The upper bound of each plot is the boundary between the reservoir and the basement located at $x_3 = 0$ km, while the lower bound is at $x_3 = -1$ km. The dash line in each subplot of $\Delta\tau$ represents the end of injection at $\Delta t = 30$ days.

For the isolated faults shown in Figures 9b and 9c, positive $\Delta\tau$ develops above $x_3 = -0.2$ km, where there is no fault, due to pore pressure diffusion into basement rocks. In the isolated/conductive case (Figure 9b),

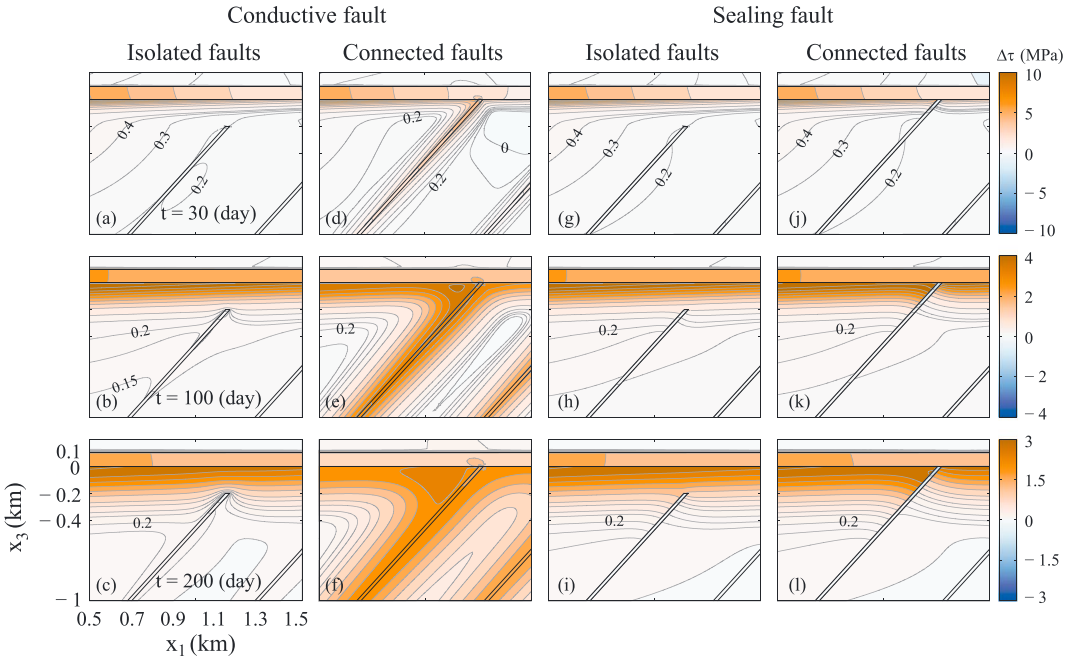

Figure 8. Coulomb stress including pore pressure change, $\Delta\tau(\mathbf{x})$, from coupled poroelasticity model at t = 30, 100, and 200 days: (a–f) conductive and (g–l) sealing faults.

pore pressure changes are limited by the duration of injection and the basement permeability. In the isolated/sealing case (Figure 9c), the low permeability of the fault limits pore pressure increases within the fault. In both of these cases, Coulomb stress changes on the fault are dominated by poroelastic effects, which are destabilizing after shut-in. For the conductive, hydraulically connected fault in Figure 9e, direct pore pressure diffusion leads to large changes in Coulomb stress. After the end of injection, pore fluid continues to diffuse and the maximum pore pressure decreases. For the sealing fault shown in Figure 9f, positive $\Delta\tau$ develops at the end of injection caused by poroelastic extension of deep basement rocks, although negative $\Delta\tau$, driven by poroelastic compression due to pressurization of adjacent basement rocks, develops at shallower depths

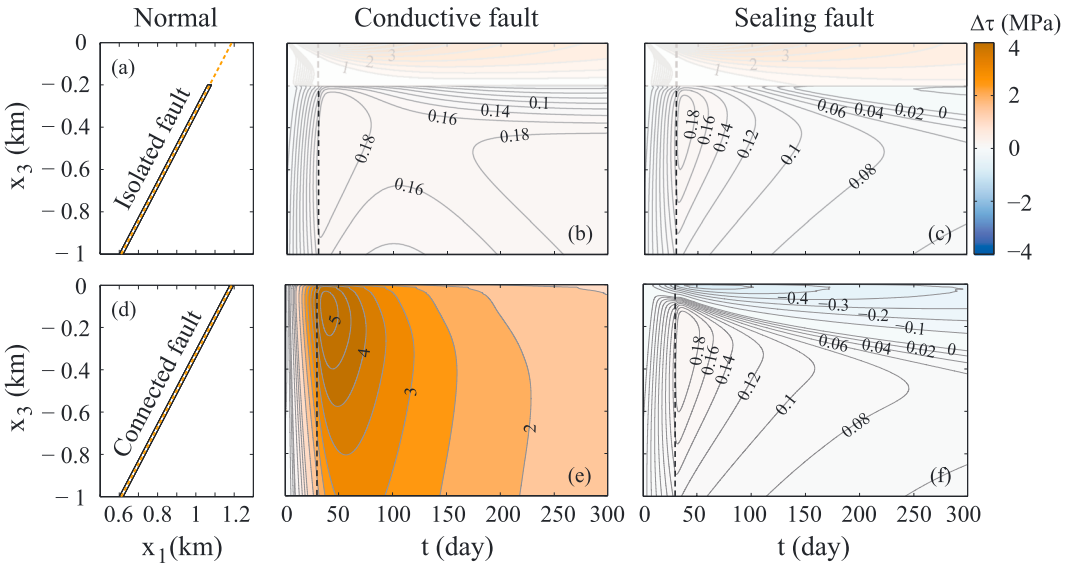

Figure 9. Coulomb stress change $\Delta\tau(t)$ in the middle of the fault nearest the injection well, as a function of position and time. (a and d) Fault geometry; stresses are computed along dashed orange lines. (b) Hydraulically isolated conductive fault, (c) hydraulically isolated sealing fault, (e) hydraulically connected conductive fault, and (f) sealing fault connected to a target reservoir.

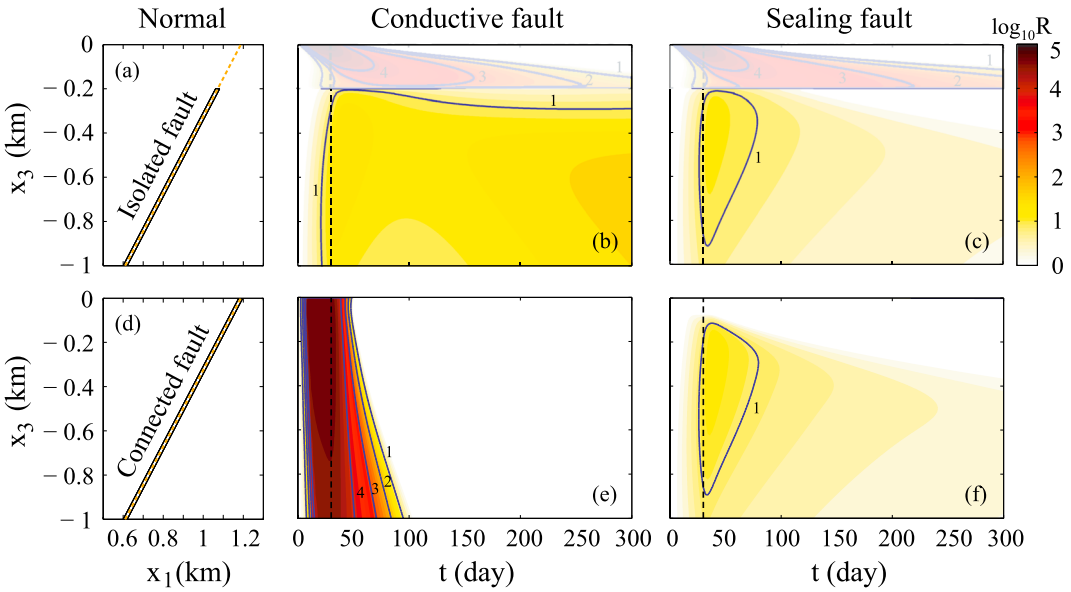

Figure 10. Seismicity rate $R(t)$ along fault nearest the injection well as a function of time, assuming normal faulting: (a and d) fault geometry; seismicity rates are calculated along dashed orange lines, (b) hydraulically isolated conductive fault, (c) hydraulically isolated sealing fault, (e) hydraulically connected conductive fault, and (f) sealing fault connected to a target reservoir.

with time driven by pore pressure diffusion into the basement. These results show that poroelastic stressing can destabilize basement faults even without direct pore pressure diffusion into them.

3.4. Seismicity Rate Prediction

Given pore pressure and stresses from the numerical simulations, we predict the seismicity rate for each scenario by solving the seismicity rate equation (20). In these calculations we assume that earthquakes occur only on preexisting fault zones, not in the unfaulted basement.

Figure 10 shows the temporal evolution of seismicity rate on a logarithmic scale, $\log_{10}R(\mathbf{x}, t)$, based on stress and pore pressure in the middle of the fault nearest the injector, for the assumed values of t_a and background stressing rate. Seismicity in unfaulted basement is muted in the figure. The dash line in each plot represents the end of injection ($\Delta t = 30$ days).

For the isolated fault shown in Figures 10b and 10c, the seismicity rate increases on the fault ($x_3 < -0.2$ km) are modest in these scenarios. The increase in R within the isolated fault zone occurs due to (1) postinjection diffusion of pore pressure, if the fault has high permeability (Figure 10b), and (2) poroelastic stressing (Figures 10b and 10c). These processes are controlled by the basement permeability, and distance between the reservoir and faults, as well as the injection rate and duration. Postinjection diffusion into the conductive fault causes a gradual increase of R in the fault without hydraulic connectivity to the target reservoir.

For the connected/conductive fault shown in Figure 10e, direct pore pressure diffusion into the fault leads to large increases in seismicity rate ($\log_{10}R > 4$, for these parameters) throughout the fault zone. On the other hand, the low permeability of the sealing fault impedes diffusion into the fault (Figure 10f). Fault normal compression on the shallow fault (-0.1 km $< x_3 < 0$ km) suppresses seismicity there. However, poroelastic extension on the lower portion of the fault ($x_3 < -0.1$ km) leads to modest increases in seismicity rate ($\log_{10}R \approx 1$, for these parameters) at depth. These results show that changes in pore pressure and/or stresses can induce seismicity in any type of basement fault. Limited diffusion into sealing faults results in negligible pore pressure change within them, but poroelastic stressing can increase the Coulomb stress, inducing seismicity.

The predicted seismicity rate depends on the perturbation in pore pressure and stress, as well as the characteristic decay time t_a [*Segall and Lu*, 2015]. Figures 11a–11c illustrate the effect of t_a on the spatiotemporal distribution of seismicity rate $\log_{10}R(\mathbf{x}, t)$ in the middle of the isolated/sealing fault for $t_a = 2$, 10, and 50 (reference case) years. With shorter t_a poroelastic stressing can induce considerable seismicity in the sealing fault zone without direct pore pressure increase, such that $\log_{10}R > 3$ for this scenario. Figure 11d shows the temporal

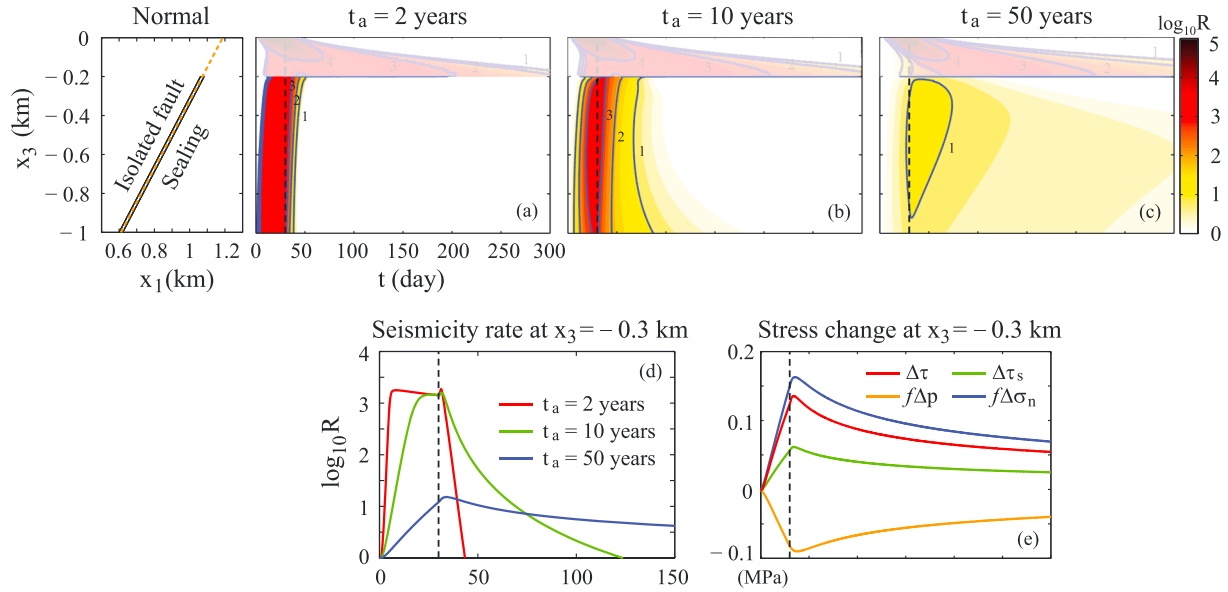

Figure 11. Seismicity rate $R(t)$ on isolated/sealing fault for different characteristic decay times t_a: (a) $t_a = 2$ years, (b) $t_a = 10$ years, and (c) $t_a = 50$ years (reference case). (d) Seismicity rate at a depth of $x_3 = -0.3$ km, where direct pore pressure change is negligible for three values of t_a. (e) Components of Coulomb stress change $\Delta\tau$ at $x_3 = -0.3$ km. Dash line indicates the end of injection.

evolution of the seismicity rate at a depth of $x_3 = -0.3$ km. For both $t_a = 2$ years and $t_a = 10$ years, the seismicity rate reaches steady state before the end of injection. A slight postinjection peak in R is observed (red and green lines in Figure 11d). *Segall and Lu* [2015] show that for injection into a homogeneous poroelastic medium, poroelastic coupling effects can in some circumstances lead to localized increases in seismicity rate post shut-in.

For the reference case $t_a = 50$ years, the seismicity rate steadily increases during injection, and the maximum seismicity rate occurs in the postinjection period (blue line in Figure 11d). The amplitude of the postinjection maximum seismicity rate decreases with the increase in t_a. Figure 11e shows the poroelastic stress changes at the same depth. During injection both the shear and normal stresses increase ($\Delta\tau_s > 0$ and $f\Delta\sigma_n > 0$), and thus, the fault is positively stressed. Because of the low permeability, pore fluid does not diffuse into the sealing fault. Perhaps surprisingly, the pore pressure there decreases due to extensional mean normal stresses. Thus, $f\Delta p$ actually reduces the Coulomb stress change. Following shut-in, the stresses continue to increase causing the peak in Coulomb stress and hence seismicity rate at this location to occur postinjection.

4. Discussion

Our numerical results show that poroelastic stressing can induce seismicity on basement faults, an effect which cannot be determined by standard uncoupled diffusion models used in many previous studies. We have presented methodology to estimate seismicity rate including poroelastic coupling that will allow others to examine alternative scenarios with variation in mechanical and hydrological parameters and/or geometries of the fault zones. We also provide a physical understanding of the sign of poroelastic effects, so that we understand at a fundamental level whether poroelastic stresses stabilize or destabilize basement faults given a particular geometry. In this section we extend our results by varying fault parameters, i.e., faulting regime and fault friction coefficient, which determine the Coulomb stress change on the faults.

4.1. Faulting Regime

As briefly mentioned in section 3.3, whether or not poroelastic stresses favor slip depends on the fault geometry and sense of slip. In calculations here with extensional (normal) faults the induced shear stresses generally favor slip on faults beneath the reservoir except for highly conductive, well-connected faults. On the other hand, for compressional (reverse) faults the induced shear stresses τ_s acts to decrease the Coulomb stress change.

Figure 12 shows the temporal evolution of the seismicity rate for the four different fault types as in Figure 10, but for reverse faulting. For conductive faults (Figures 12b and 12e) pore pressure diffusion causes an

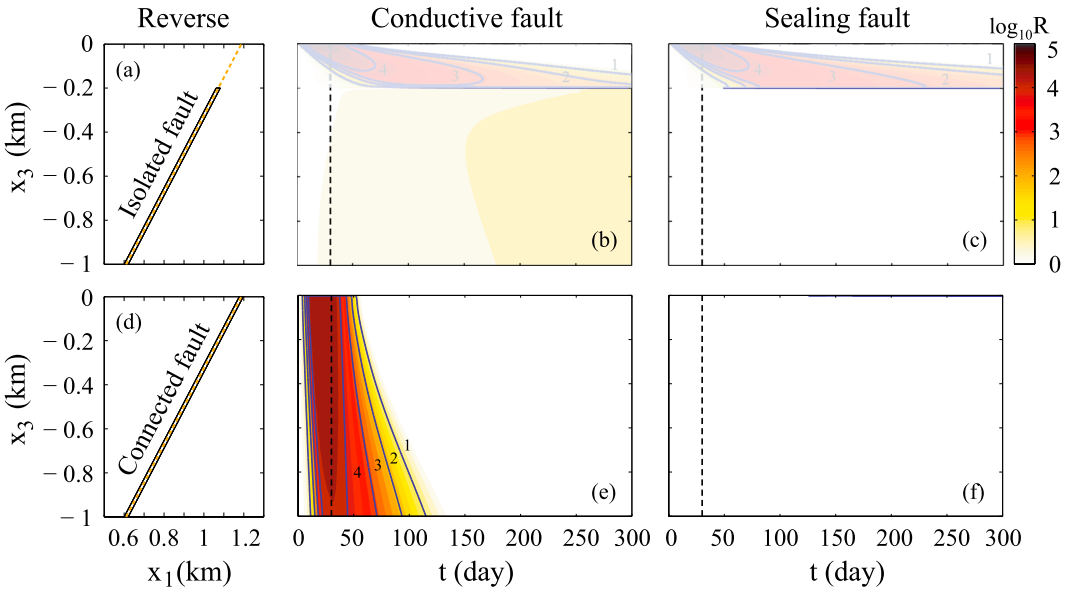

Figure 12. Seismicity rate $R(t)$ on fault nearest the injection well under reverse faulting conditions: (a and d) fault geometry; seismicity rates are calculated along dashed orange lines, (b) hydraulically isolated conductive fault, (c) hydraulically isolated sealing fault, (e) hydraulically connected conductive fault, and (f) sealing fault connected to a target reservoir.

increase in seismicity rate, but of smaller magnitude than in the normal faulting geometry. For sealing faults (Figures 12c and 12f) there is no induced seismicity, since poroelastic stressing inhibits slip.

4.2. Uncertainty in Fault Friction

The static friction coefficient f in this study was assumed to have a standard laboratory value of $f = 0.75$. Measurements from deep boreholes have confirmed that static friction coefficients of fault zone materials are often in the range 0.6–1.0, in agreement with laboratory values [*Zoback and Healy*, 1992; *Brudy et al.*, 1997]. However, some minerals have much lower friction coefficients [*Saffer et al.*, 2001; *Collettini et al.*, 2009; *Ikari et al.*, 2009; *Lockner et al.*, 2011; *Di Toro et al.*, 2011].

With low friction coefficient, shear stress changes play a more significant role in fault failure. Figure 13 shows the temporal evolution of the poroelastic stress change $\Delta\tau_s + f\Delta\sigma_n$ for $f = 0.1$. For the reference case of $f = 0.75$, we observe negative poroelastic stress changes on the upper fault and positive changes, up to 0.06 MPa, on the lower fault during injection (Figure 13a). For $f = 0.1$, on the other hand, we observe positive changes in poroelastic stress, up to 1.4 MPa, due to a reduced contribution from $\Delta\sigma_n$ (Figure 13b). Note that a reduction in friction coefficient also reduces the direct pore pressure effect $f\Delta p$. This result emphasizes that poroelastic stress effects depend not only on fault geometry and sense of slip but also on fault zone frictional properties.

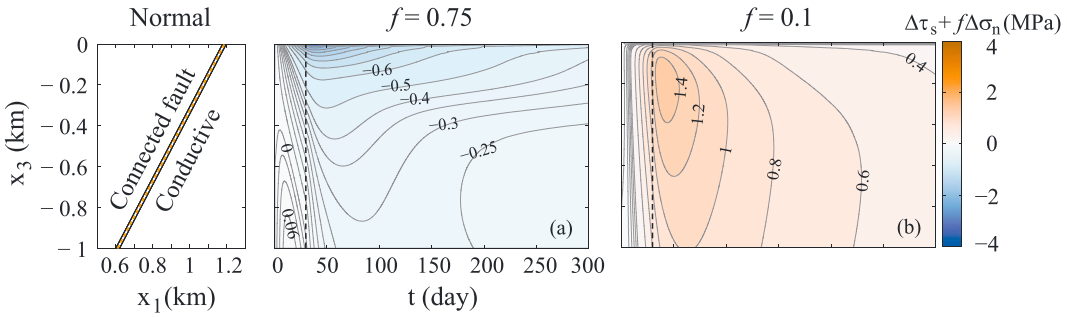

Figure 13. Poroelastic stress $\Delta\tau_s + f\Delta\sigma_n$ in the middle of a conductive fault hydraulically connected to the target reservoir, with friction coefficient f: (a) $f = 0.75$ (reference case) and (b) $f = 0.1$.

5. Conclusion

Including full poroelastic coupling effects predicts larger pore pressures within the target formation compared to an uncoupled flow model. This pore pressure increase is compensated by compressive mean normal stresses. In a layered system, injection-induced pore pressures dissipate into basement rocks modifying the stress state. Both direct pore pressure changes and poroelastic stressing perturb basement faults potentially inducing seismicity.

For conductive faults hydraulically connected to the target formation, rapid diffusion into the faults leads to large increases in Coulomb stress and potentially significant seismicity. If faults are isolated from the target formation, pore pressure perturbations may ultimately diffuse into basement faults, depending on basement diffusivity and injection history. For sealing (low-permeability) faults, direct pore pressure increases are limited. However, elevated pore pressure in the surrounding basement creates pore pressure gradients which generate poroelastic stresses that, in some cases, can promote slip. In the lower portion of the faults, beyond the direct effect of elevated pore pressure, increases in Coulomb stress caused solely by poroelastic expansion of the reservoir may promote faulting, depending on fault orientation and background stress state.

We estimate the seismicity rate relative to the background rate on basement faults using the seismicity rate model of *Dieterich* [1994] including poroelastic stress changes. Both the fault permeability and its connectivity to the target formation determine the seismicity rate on each fault type. Our results suggest that induced seismicity occurs on basement faults by two mechanisms: (1) direct diffusion into conductive faults, with or without hydraulic connectivity to the target formation, and (2) indirect stress changes due to poroelastic stressing. The largest seismicity rates are developed in the hydraulically connected/conductive faults due to direct pore pressure diffusion, while smaller increases in seismicity rate may occur on isolated faults, solely due to poroelastic stressing, depending on whether induced shear and normal stresses favor fault slip. The accumulation of pore pressure in the basement adjacent to sealing faults causes pore pressure gradients that may induce seismicity, depending on fault geometry.

For the fault geometry examined here, with high-angle normal faults beneath the reservoir, poroelastic stresses generally favor slip. For the same geometry poroelastic stresses inhibit slip in reverse faulting environments. Lower friction coefficients lead to higher seismicity rates, for hydraulically isolated normal faults.

Appendix A: Computation of Coulomb Stressing Rate

To solve for seismicity rate, equation (20), requires the Coulomb stressing rate $\dot{\tau} = \dot{\tau}_s + f(\dot{\sigma}_n + \dot{p})$. We obtain $\tau(\mathbf{x}_l, t_m)$ at discrete locations and times from the two-dimensional finite element model. Then, we use cubic smoothing splines to generate a stress history that can be differentiated to yield $\dot{\tau}(\mathbf{x}_l, t_k)$ for all t_k. The interpolating spline approximates a smooth function $f(t_m)$ with data points $(\tau(\mathbf{x}_l, t_m), t_m)$. The spline function $F(t_m) = F_m$ minimizes the functional

$$L = \omega \sum_{m=0}^{n} \left(\frac{y_m - F_m}{\sigma_m} \right)^2 + (1-\omega) \int_{t_0}^{t_n} \left(F_m'' \right)^2 \mathrm{d}t, \tag{A1}$$

where y_m is the data value approximated by the equation $y_m = f(t_m) + \pi_m$, where π_m form a sequence of independently distributed random variables with the standard deviation σ_m^2. The smoothing parameter ω determines the relative weight for smoothness versus data fit; a reasonable value for ω is near $1/(1 + h^3/6)$ where $h = t_{m+1} - t_m$ the spacing of the stress data. In order to validate our approximation of $\dot{\tau}(\mathbf{x}_l, t_k)$, we compare $\dot{\tau}(\mathbf{x}_l, t_k)$ from numerical modeling of a homogeneous domain with the analytical derivatives of the *Rudnicki* [1986] solutions obtained by *Segall and Lu* [2015]. This validation confirmed the accuracy of the smoothing procedure.

The ordinary differential equation (20) is solved using `ode45` in which the stress rate is computed as follows:

1. Compute $\tau(\mathbf{x}_l, t_m) = \tau_s(\mathbf{x}_l, t_m) + f[\sigma_n(\mathbf{x}_l, t_m) + p(\mathbf{x}_l, t_m)]$ at each element and numerical time step from the COMSOL output.
2. Use cubic smoothing splines to compute $\tau(\mathbf{x}_l, t_k)$ at arbitrary time t_k using `csaps` in MATLAB.
3. Differentiate the stress interpolant to yield $\dot{\tau}(\mathbf{x}_l, t_k)$ using `fnder` in MATLAB.

Appendix B: Fluid Increment in Terms of Poroelastic Coefficients

Fluid exchange within a control volume can be due to deformation, change of pore pressure, or the presence of a source or sink. The second poroelastic constitutive equation (2) relates the increment of fluid mass to the linear combination of mean stress σ_{kk} and pore pressure p. Using the relation between the Skempton's coefficient B and Biot-Willis coefficient α [*Segall*, 2010],

$$B = \frac{3(\nu_u - \nu)}{\alpha(1-2\nu)(1+\nu_u)}, \tag{B1}$$

the constitutive equation (2) can be expressed in terms of the unconstrained specific storage S_σ defined as (9)

$$\Delta m = \rho_f S_\sigma \left(\frac{B}{3}\sigma_{kk} + p\right). \tag{B2}$$

Under uniaxial strain and constant vertical stress conditions ($\epsilon_{11} = \epsilon_{22} = 0, \sigma_{33} = 0$), the constitutive equation (1) yields

$$0 = \left[\sigma_{11} - \frac{\nu}{1+\nu}(\sigma_{11}+\sigma_{22}) + \frac{1-2\nu}{1+\nu}\alpha p\right], \tag{B3}$$

$$0 = \left[\sigma_{22} - \frac{\nu}{1+\nu}(\sigma_{11}+\sigma_{22}) + \frac{1-2\nu}{1+\nu}\alpha p\right]. \tag{B4}$$

Using these relations, we can have

$$\sigma_{kk} = \sigma_{11} + \sigma_{22} = -\frac{2(1-2\nu)}{1-\nu}\alpha p. \tag{B5}$$

This shows that the change in mean stress is a scalar multiple of the change in pore pressure for uniaxial strain and constant vertical stress conditions, which implies that the stress field uncouples from the pore pressure field. Substituting (B5) into (B2),

$$\Delta m = \rho_f S_u p. \tag{B6}$$

Then, we can calculate the injection-induced change in fluid mass using the relations (B2) and (B6) for both coupled and uncoupled models as follows

$$\Delta m = \begin{cases} \rho_f S_\sigma \left(\frac{B}{3}\sigma_{kk} + p\right) & ; \text{ coupled} \\ \rho_f S_u p & ; \text{ uncoupled} \end{cases}. \tag{B7}$$

Acknowledgments
We thank the reviewers for their very helpful comments that substantially improved the manuscript. This work was supported by the Stanford Center for Induced and Triggered Seismicity. No data were used in producing this manuscript.

References

Bacon, D., N. Qafoku, Z. Dai, E. Keating, and C. Brown (2016), Modeling the impact of carbon dioxide leakage into an unconfined, oxidizing carbonate aquifer, *Int. J. Greenhouse Gas Control*, *44*, 290–299, doi:10.1016/j.ijggc.2015.04.008.

Beeler, N. M., and D. A. Lockner (2003), Why earthquakes correlate weakly with the solid Earth tides: Effects of periodic stress on the rate and probability of earthquake occurrence, *J. Geophys. Res.*, *108*(B8), 2391, doi:10.1029/2001JB001518.

Bense, V. F., and M. A. Person (2006), Faults as conduit-barrier systems to fluid flow in siliciclastic sedimentary aquifers, *Water Resour. Res.*, *42*, W05421, doi:10.1029/2005WR004480.

Biot, M. A. (1941), General theory of three-dimensional consolidation, *J. Appl. Phys.*, *12*, 155–164.

Birkholzer, J. T., Q. Zhou, and C. F. Tsang (2009), Large-scale impact of CO_2 storage in deep saline aquifer: A sensitivity study on pressure response in stratified systems, *Int. J. Greenhouse Gas Control*, *3*(2), 181–194.

Brudy, M., M. D. Zoback, F. R. K. Fuchs, and J. Baumgartner (1997), Estimation of the complete stress tensor to 8 km depth in the KTB scientific drill holes: Implications for crustal strength, *J. Geophys. Res.*, *102*(B8), 18,453–18,475, doi:10.1029/96JB02942.

Chang, K. W., and S. L. Bryant (2009), The effect of faults on dynamics of CO_2 plumes, *Energy Procedia*, *1*(1), 1839–1846.

Chang, K. W., M. A. Hesse, and J. P. Nicot (2013), Reduction of lateral pressure propagation due to dissipation into ambient mudrocks during geological carbon dioxide storage, *Water Resour. Res.*, *49*, 2573–2588, doi:10.1002/wrcr.20197.

Cocco, M., and J. R. Rice (2002), Pore pressure and poroelasticity effects in Coulomb stress analysis of earthquake interactions, *J. Geophys. Res.*, *107*(B2), 2030, doi:10.1029/2000JB000138.

Collettini, C., A. Niemeijer, C. Viti, and C. Marone (2009), Fault zone fabric and fault weakness, *Nature*, *462*, 907–901, doi:10.1038/nature08585.

COMSOL (2014), *COMSOL Multiphysics User's Guide*, COMSOL AB, Burlington, Mass.

Dai, Z., P. H. Stauffer, J. W. Carey, R. S. Middleton, Z. Lu, J. F. Jacobs, K. Hnottavange-Telleen, and L. H. Spangler (2014), Pre-site characterization risk analysis for commercial-scale carbon sequestration, *Environ. Sci. Technol.*, *48*(7), 3908–3915, doi:10.1021/es405468p.

Di Toro, G., R. Han, T. Hirose, N. D. Paola, S. Nielsen, K. Mizoguchi, F. Ferri, M. Cocco, and T. Shimamoto (2011), Fault lubrication during earthquakes, *Nature*, *471*, 494–498, doi:10.1038/nature09838.

Dieterich, J. H. (1979), Modeling of rock friction: 1. Experimental results and constitutive equations, *J. Geophys. Res.*, *84*, 2161–2168, doi:10.1029/JB084iB05p02161.
Dieterich, J. H. (1986), A model for the nucleation of earthquake slip, in *Earthquake Source Mechanics*, edited by S. Das, J. Boatwright, and C. H. Scholz, pp. 37–47, AGU, Washington, D. C.
Dieterich, J. H. (1994), A constitutive law for rate of earthquake production and its application to earthquake clustering, *J. Geophys. Res.*, *99*(B2), 2601–2618, doi:10.1029/93JB02581.
Dieterich, J. H., and B. D. Kilgore (1994), Direct observation of frictional contacts: New insights for state-dependent properties, *Pure Appl. Geophys.*, *143*(1–3), 283–302, doi:10.1007/BF00874332.
Dreij, K., Q. A. Chaudhry, B. Jernstrom, R. Morgenstern, and M. Hanke (2011), A method for efficient calculation of diffusion and reactions of lipophilic compounds in complex cell geometry, *PLoS One*, *6*(8), 1–18.
Ellsworth, W. L. (2013), Injection-induced earthquakes, *Science*, *341*(6142), 1225942, doi:10.1126/science.1225942.
Frohlich, C., W. L. Ellsworth, W. A. Brown, M. Brunt, J. H. Luetgert, T. MacDonald, and S. Walter (2014), The 17 May 2012 M4.8 earthquake near Timpson, East Texas: An event possibly triggered by fluid injection, *J. Geophys. Res. Solid Earth*, *119*, 581–593, doi:10.1002/2013JB010755.
Green, D. H., and H. F. Wang (1990), Specific storage as a poroelastic coefficient, *Water Resour. Res.*, *26*(7), 1631–1637, doi:10.1029/WR026i007p01631.
Harris, R. A., R. W. Simpson, and P. A. Reasenberg (1995), Influence of static stress changes on earthquake locations in southern California, *Nature*, *375*, 221–224, doi:10.1038/375221a0.
Healy, J. H., W. Rubey, D. Griggs, and C. Raleigh (1968), The Denver earthquakes, *Science*, *161*(3848), 1301–1310, doi:10.1126/science.161.3848.1301.
Horton, S. (2012), Disposal of hydrofracking waste water fluid by injection into subsurface aquifers triggers earthquake swarm in central Arkansas with potential for damaging earthquake, *Seismol. Res. Lett.*, *83*(2), 250–260, doi:10.1785/gssrl.83.2.250.
Hughes, T. J. R. (2000), *The Finite Element Method: Linear Static and Dynamic Finite Element Analysis*, Courier Dover Publ., Mineola, New York.
Ikari, M. J., D. M. Saffer, and C. Marone (2009), Frictional and hydrologic properties of clay-rich fault gouge, *J. Geophys. Res.*, *114*, B05409, doi:10.1029/2008JB006089.
Jaeger, J. C., and N. G. W. Cook (1979), *Fundamentals of Rock Mechanics*, Chapman and Hall, London, U. K.
Jha, B., and R. Juanes (2014), Coupled multiphase flow and poromechanics: A computational model of pore pressure effects on fault slip and earthquake triggering, *Water Resour. Res.*, *50*, 3776–3808, doi:10.1002/2013WR015175.
Kerenan, K. M., H. M. Savage, G. A. Abers, and E. S. Cochran (2013), Potentially induced earthquakes in Oklahoma, USA: Links between wastewater injection and the 2011 M_w 5.7 earthquake sequence, *Geology*, *41*, 699–702, doi:10.1130/G34045.1.
Kerenan, K. M., M. Weingarten, G. A. Abers, B. Bekins, and S. Ge (2014), Sharp increase in central Oklahoma seismicity since 2008 induced by massive wastewater injection, *Science*, *345*(6195), 448–451, doi:10.1126/science.1255802.
Kim, S., and S. Hosseini (2013), Above-zone pressure monitoring and geomechanical analyses for a field-scale CO_2 injection project, Cranfield, MS, *Greenhouse Gases Sci. Technol.*, *4*, 81–98.
Kim, W. Y. (2013), Induced seismicity associated with fluid injection into a deep well in Youngstown, Ohio, *J. Geophys. Res. Solid Earth*, *118*, 3506–3518, doi:10.1002/jgrb.50247.
Lockner, D., C. Morrow, D. Moore, and S. Hickman (2011), Low strength of deep San Andreas fault gouge from SAFOD core, *Nature*, *472*, 82–85, doi:10.1038/nature09927.
Narasimhan, T., and B. Kanehiro (1980), A note on the meaning of storage coefficient, *Water Resour. Res.*, *16*, 423–429, doi:10.1029/WR016i002p00423.
Nicholson, C., and R. L. Wesson (1990), Earthquake hazard associated with deep well injection: A report to the U.S. Environmental Protection Agency, *Tech. Rep.*, U.S. Geol. Surv. Bull., Reston, Va.
NRC (2013), *Induced Seismicity Potential in Energy Technologies*, Natl. Acad. Press, Washington, D. C.
Raleigh, C. B., J. H. Healy, and J. D. Bredehoeft (1976), An experiment in earthquake control at Rangely, Colorado, *Science*, *191*(4233), 1230–1237, doi:10.1126/science.191.4233.1230.
Rice, J. R., and M. P. Cleary (1976), Some basic stress diffusion solutions for fluid-saturated porous media with compressible constituents, *Rev. Geophys.*, *14*, 227–241, doi:10.1029/RG014i002p00227.
Rinaldi, A. P., P. Jeanne, J. Rutqvist, F. Cappa, and Y. Guglielmi (2014), Effects of fault-zone architecture on earthquake magnitude and gas leakage related to CO_2 injection in a multi-layered sedimentary system, *Greenhouse Gases Sci. Technol.*, *4*(1), 99–120.
Rothert, E., and S. A. Shapiro (2003), Microseismic monitoring of borehole fluid injections: Data modeling and inversion for hydraulic properties of rocks, *Geophysics*, *68*(2), 685–689.
Rubinstein, J. L., and A. B. Mahani (2015), Myths and facts on wastewater injection, hydraulic fracturing, enhanced oil recovery, and induced seismicity, *Seismol. Res. Lett.*, *86*(4), 1060–1067, doi:10.1785/0220150067.
Rudnicki, J. W. (1986), Fluid mass sources and point forces in linear elastic diffusive solids, *Mech. Mater.*, *5*(4), 383–393, doi:10.1016/0167-6636(86)90042-6.
Saffer, D., K. M. Frye, C. Marone, and K. Mair (2001), Laboratory results indicating complex and potentially unstable frictional behaviour of smectite clay, *Geophys. Res. Lett.*, *28*(12), 2297–2300, doi:10.1029/2001GL012869.
Seeber, L., and J. G. Armbruster (1993), Natural and induced seismicity in the Lake Erie-Lake Ontario region: Reactivation of ancient faults with little neotectonic displacement, *Geogr. Phys. Quatern.*, *47*(3), 363–378.
Seeber, L., J. G. Armbruster, and W. Y. Kim (2004), A fluid injection-triggered earthquake sequence in Ashtabula, Ohio: Implications for seismogenesis in stable continental regions, *Bull. Seismol. Soc. Am.*, *94*(1), 76–87.
Segall, P. (1985), Stress and subsidence resulting from subsurface fluid withdrawal in the epicentral region of the 1983 Coalinga earthquake, *J. Geophys. Res.*, *90*(B8), 6801–6816, doi:10.1029/JB090iB08p06801.
Segall, P. (1989), Earthquakes triggered by fluid extraction, *Geology*, *17*(10), 942–946, doi:10.1130/0091-7613.
Segall, P. (2010), *Earthquake and Volcano Deformation*, Princeton Univ. Press, Princeton, N. J.
Segall, P., and S. Lu (2015), Injection induced seismicity: Poroelastic and earthquake nucleation effects, *J. Geophy. Res. Solid Earth*, *120*, 5082–5103, doi:10.1002/2015JB012060.
Segall, P., J.-R. Grasso, and A. Mossop (1994), Poroelastic stressing and induced seismicity near the Lacq gas field, southwestern France, *J. Geophys. Res.*, *99*(B8), 15,423–15,438, doi:10.1029/94JB00989.
Shapiro, S. A., and C. Dinske (2009), Fluid-induced seismicity: Pressure diffusion and hydraulic fracturing, *Geophys. Prospect.*, *57*(2), 301–310, doi:10.1111/j.1365-2478.2008.00770.x.
Shapiro, S. A., E. Huenges, and G. Borm (2007), Estimating the crust permeability from fluid-injection-induced seismic emission at the KTB site, *Geophys. J. Int.*, *131*(2), 15–18, doi:10.1111/j.1365-246X.1997.tb01215.x.

Stanislavsky, E., and G. Garven (2002), The minimum depth of fault failure in compressional environments, *Geophys. Res. Lett.*, *29*(24), 2155, doi:10.1029/2002GL016363.

Tsang, C.-F., and J. A. Apps (2005), Underground injection science and technology, in *Developments in Water Sciences*, vol. 52, edited by C.-F. Tsang and J. A. Apps, pp. 327–339, Elsevier, Amsterdam.

Tueckmantel, C., Q. J. Fisher, T. Manzocchi, S. Skachkov, and C. A. Grattoni (2012), Two-phase fluid flow properties of cataclastic fault rocks: Implications for CO_2 storage in saline aquifers, *Geology*, *40*, 39–42, doi:10.1130/G32508.1.

U.S. Environmental Protection Agency (2010), Federal Requirements under the Underground Injection Control (UIC) Program for Carbon Dioxide (CO_2) Geologic Sequestration (GS) Wells, Federal Register 75 FR 77230.

Vilarrasa, V., and J. Carrera (2015), Geologic carbon storage is unlikely to trigger large earthquakes and reactivate faults through which CO_2 could leak, *Proc. Natl. Acad. Sci. U.S.A.*, *112*(19), 5938–5943, doi:10.1073/pnas.1413284112.

Wang, H. F. (2000), *Theory of Linear Poroelasticity*, Princeton Univ. Press, Princeton, N. J.

Willson, J. P., R. J. Lunn, and Z. K. Shipton (2007), Simulating spatial and temporal evolution of multiple wing cracks around faults in crystalline basement rocks, *J. Geophys. Res.*, *112*, B08408, doi:10.1029/2006JB004815.

Zhang, Y., et al. (2013), Hydrogeologic controls on induced seismicity in crystalline basement rocks due to fluid injection into basal reservoirs, *Ground Water*, *51*(4), 525–538, doi:10.1111/gwat.12071.

Zoback, M. D., and S. M. Gorelick (2012), Earthquake triggering and large-scale geologic storage of carbon dioxide, *Proc. Natl. Acad. Sci. U.S.A.*, *109*(26), 10,164–10,168, doi:10.1073/pnas.1202473109.

Zoback, M. D., and J. H. Healy (1992), In situ stress measurements to 3.5 km depth in the Cajon Pass Scientific Research Borehole: Implications for the mechanics of crustal faulting, *J. Geophys. Res.*, *97*(B4), 5039–5057, doi:10.1029/91JB02175.